

High Repetition-Rate Wakefield Electron Source Generated by Few-millijoule, 30 Femtosecond Laser Pulses on a Density Downramp

Z.-H He, B Hou, J A Nees, J H Easter, Jérôme Faure, K Krushelnick, a G R

Thomas

▶ To cite this version:

Z.-H He, B Hou, J A Nees, J H Easter, Jérôme Faure, et al.. High Repetition-Rate Wakefield Electron Source Generated by Few-millijoule, 30 Femtosecond Laser Pulses on a Density Downramp. New Journal of Physics, 2013, 15, pp.053016. hal-01159032

HAL Id: hal-01159032 https://ensta-paris.hal.science/hal-01159032

Submitted on 2 Jun 2015 $\,$

HAL is a multi-disciplinary open access archive for the deposit and dissemination of scientific research documents, whether they are published or not. The documents may come from teaching and research institutions in France or abroad, or from public or private research centers. L'archive ouverte pluridisciplinaire **HAL**, est destinée au dépôt et à la diffusion de documents scientifiques de niveau recherche, publiés ou non, émanant des établissements d'enseignement et de recherche français ou étrangers, des laboratoires publics ou privés.

High Repetition-Rate Wakefield Electron Source Generated by Few-millijoule, 30 Femtosecond Laser Pulses on a Density Downramp

Z.-H. He¹, B. Hou¹, J. A. Nees¹, J. H. Easter¹, J. Faure², K. Krushelnick¹ and A. G. R. Thomas¹

 1 Center for Ultrafast Optical Science, University of Michigan, Ann Arbor, MI 48109-2099 USA

² Laboratoire d'Optique Appliquée, ENSTA-CNRS-Ecole Polytechnique, UMR 7639, 91761 Palaiseau, France

Abstract. We report on an experimental demonstration of laser wakefield electron acceleration using a sub-TW power laser by tightly focusing 30-fs laser pulses with 8 mJ pulse energy on a 100 μ m scale gas target. The experiments are carried out at an unprecedented 0.5 kHz repetition rate, allowing "real time" optimization of accelerator parameters. Well-collimated and stable electron beams with quasi-monoenergetic peaks around 100 keV are measured. Particle-in-cell simulations show excellent agreement with the experimental results and suggest an acceleration mechanism based on electron trapping on the density downramp, due to the time varying phase velocity of the plasma waves.

PACS numbers: 41.75.Jv, 52.38.Kd, 52.65.Rr, 29.25.Bx

Submitted to: New J. Phys.

1. Introduction

Since the concept of laser driven plasma accelerators was first proposed by Tajima and Dawson [1], advances in high-power ultrafast laser technology have enabled successful production of energetic electron beams in numerous wakefield acceleration experiments [2–14]. Plasma-based particle acceleration holds significant promise for future compact sources of relativistic electron beams because of the large acceleration gradients plasma can sustain relative to conventional radio frequency cavities. A high intensity laser pulse propagating in an underdense plasma generates large amplitude plasma waves with phase velocities close to the speed of light. Under certain conditions, electrons can be trapped in the waves and accelerated to relativistic energies. Recent progress has demonstrated that using ultrashort laser pulses, ultra-relativistic electrons with quasi-monoenergetic spectra ($\Delta E/E < 5\%$ [2, 3, 5]), small transverse emittance (< 1 π mm mrad [6]), up to GeV energies [7–9] can be generated in a stable accelerating structure in the so-called the "blowout" or "bubble" regime [15].

Accelerating electrons in the blowout regime requires a laser pulse that is both intense (with $a_0 > 1$, where $a_0 = eA/m_ec$ is the normalized vector potential) and short (with pulse duration $\tau \leq 2\pi c/\omega_p$, where $\omega_p = \sqrt{e^2 n_e/m_e\epsilon_0}$ is the plasma frequency). In typical experiments, the intense laser pulse is focused onto the edge of a supersonic gas jet with a matched spot size. The densities of such gaseous targets, typically providing electron plasma densities around 10^{19} cm^{-3} indicate that short-pulse (~30 fs) laser systems with pulse energies on the order of a Joule or more are necessary to reach the critical power for self-focusing. Earlier experiments using longer laser pulses also accelerated electrons via a self-modulation instability where the laser pulse length was much greater than the wavelength of a relativistic plasma wave, $\tau > 2\pi c/\omega_p$ [10–14]. However, these experiments were limited to operation at a low repetition rate (much less than 10 Hz) due to the high laser pulse energies.

Using a low energy laser pulse to accelerate electrons requires a short underdense plasma, as laser depletion in generating the plasma wave limits the acceleration length. Conditions for electron trapping in the plasma wave are also restrictive due to the lower achievable intensity. One method for trapping electrons is to use a density downramp injection mechanism [16], which was recently demonstrated experimentally using 10 TW lasers [17–19]. In this scheme, the inhomogenous plasma leads to a time varying plasma wave phase velocity, which allows trapping once the electron velocity v_e exceeds the wave phase velocity v_{ph} , $v_e > v_{ph}$.

In this paper, we report on electron acceleration in an unexplored regime of plasma wakefield driven by few-millijoule femtosecond laser pulses (sub-TW) at high repetition rate (0.5 kHz). The high repetition rate enables better statistics that has not been accessible in previous similar experiments. Collimated electron beams are produced with energies in the 100 keV range by acceleration in slow (non-relativistic) plasma waves on the density downramp of a 100 μ m scale gas target. Because of the relatively high charge (~ 10 fC) and potentially short temporal duration, such electron sources

have the potential to be used for ultrafast electron diffraction (UED) applications [20].

In conventional UED, electrons from femtosecond laser pulse induced photoemission are accelerated by an external electric field. It is a challenging problem to control broadening of electron pulses at the photocathode due to space-charge [21]. Laser plasma acceleration eliminates external acceleration instruments and also the need for a photocathode, and therefore may enable single-shot femtosecond diffraction. Recently, laser-accelerated electrons from solid target interactions have been demonstrated to successfully produce diffraction patterns from a single crystal gold sample [22]. The phase space distribution of accelerated electrons from laser driven plasma wakefield can in principle be exploited to realize compression for producing high-brightness ultrashort electron bunches. The gas target also permits operation at higher repetition rate with easier alignment and less debris.

2. Experimental results

The experiments were performed using the λ^3 laser system at the Center for Ultrafast Optical Science of the University of Michigan. This Ti:Sapphire based chirped pulse amplification (CPA) laser has a regenerative amplifier and a two-pass amplifier. It is capable of delivering pulses with energies up to 10 mJ and durations of 32 fs (FWHM) at a central wavelength of 800 nm. The output laser pulse is reflected from a deformable mirror (DM) and focused by an f/2 off-axis paraboloidal mirror to a vacuum spot size of 2.5 μ m (FWHM). The focal spot can be optimized by iteratively setting the DM so that the signal of second-harmonic generation (SHG) from a barium borate (BBO) crystal is maximized. Up to 8 mJ pulse energy is available on target, which produces a peak intensity of 3×10^{18} W/cm².

To achieve high repetition rates with the desired small diameter gas profile, we used a free flowing capillary source. The gas target was produced by flowing argon or helium gas through a fused silica capillary tubing which had an inner diameter of 100 μ m. An approximately 1 cm length of this tubing was connected to a standard compressed gas system. A motorized XYZ stage was used to manipulate the capillary tubing to an accuracy of 2 μ m. The gas flow experiences free expansion into vacuum and different plasma densities were achieved by varying the backing pressure. A Mach-Zehnder interferometer configuration, using a beam containing 2% energy split from the main beam and probing the gas flow transversely, was used to measure the plasma density profile. The interferogram data provide diagnostics on both the plasma spatial distribution and its temporal evolution, by varying the probe delay time. A 2D electron density map was reconstructed via Abel inversion of the phase-shift data as shown in figure 1.

A high resolution scintillator plate (FOS by Hamamatsu) at 32 cm downstream from the plasma or a Lanex screen at 8 cm downstream was used to record the electron beam profiles, which was imaged on a 12-bit CCD camera. The electron energy spectrum was measured using two different methods for cross calibration. In the first configuration, the

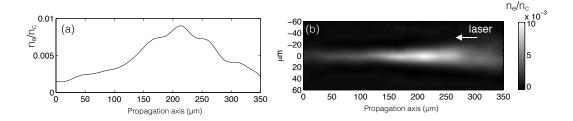


Figure 1. (a) Lineout of electron on-axis density. (b) Reconstructed electron density map.

electron energy distribution was obtained by inserting a removable electron spectrometer comprising a pair of disc magnets yoked together to provide a maximum magnetic field strength of 25 mT at the midplane. To improve the spectral resolution of the measurement, a 0.5 mm aluminum slit was mounted vertically at the magnet entrance. A pinhole located at 8 cm downstream subtending a solid angle of 80 msr was used to sample the portion of electron beam into the spectrometer. A typical spectrally dispersed electron signal is shown in figure 3(b). The absolute response of FOS plate for electrons in the range of 50-300 keV was calibrated using an electron microscope. The second configuration employed a custom built magnet spectrometer [23] equipped with an image plate (FUJI BAS-SR 2025, calibrated in [24]) [figure 3(c)]. The spectrometer has an entrance aperture with a diameter of 3 mm and a solid angle acceptance of 1 msr.

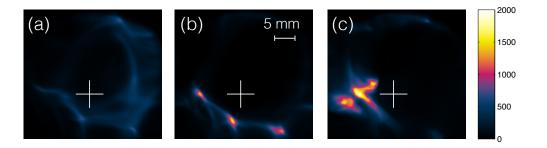


Figure 2. Typical electron beam profiles (from argon plasma) measured at 32 cm downstream. The white cross indicates the position of the laser propagation axis. The length of each arm represents a half angle of 10 mrad. These three images were taken under the same experimental conditions except the deformable mirror is (a) off (a "flat" mirror); (b) optimized for best SHG generation and (c) optimized for best electron signal. The acquisition time are 1000 ms, 1000 ms, and 200 ms respectively for (a), (b) and (c).

Typical electron beam profiles are shown in figure 2(a)-(c). The spatial distribution of the electron beam shows a "ring" structure around the laser central axis with a divergence angle about 50 mrad. By applying different DM configurations, thus changing the wavefront of laser beam, the electron beam profile can be altered and the beam charge can be optimized. An improvement of more than a factor of 10 for the maximum signal count can be achieved by feeding the electron produced signal measured on a silicon PIN diode to the deformable mirror's genetic algorithm for optimization. The structure and pointing of the electron beam remains stable once a DM configuration has been set and the vacuum chamber has reached equilibrium state. The shot-to-shot pointing stability of the beam was found to be better than 400 μ rad, which was limited by the resolution of the imaging system. The oscilloscope trace from the silicon diode consistently showed less than 10% shot-to-shot fluctuation. In the experiments, data were obtained in "real time" for optimization of the beam parameters.

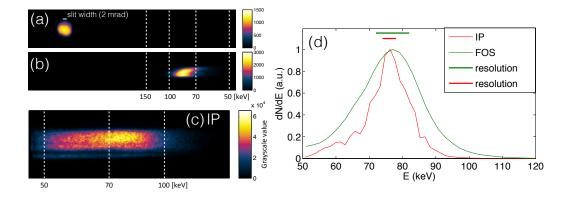


Figure 3. (a)(b): Typical spectrum data obtained with FOS plate (from argon plasma) (a) without magnets (no slit; electron beam through the pinhole) (b) spectrally dispersed electron. (c) Raw spectrum data on image plate with the custombuilt electron spectrometer under the same experimental conditions as in (b). (d) Deconvoluted electron spectra for (b) and (c) using calibrated detector response for both FOS and IP. Each horizontal bar represents the energy resolution due to the finite acceptance angle from the slit or the pinhole.

The raw images of the spectrum measurement are shown in figure 3(c)-(e) with calibration lines. The measured spectrum exhibits an energy peak in the 100 keV range with a small absolute energy spread $\Delta E_{\rm FWHM} \approx 20$ keV. For a fixed focusing position, electrons were observed over a finite range of backing pressures corresponding to plasma densities of order 10¹⁹ cm⁻³, inferred from interferometric measurement. Quantitatively similar results have been observed in the experiments using both argon and helium at comparable electron densities [figure 4(a)].

At lower densities, the plasma wave phase velocity is so high that the oscillating electrons are below the trapping threshold. At plasma densities where the plasma wavelength λ_p in the wake is comparable to the laser pulse length L, large amplitude plasma waves are resonantly excited [25], enabling strong acceleration of injected electrons. At higher densities, the laser pulse is likely to be susceptible to a plasma defocusing or filamentation instability. The electron signal in our experiments showed that electrons were preferentially accelerated when the laser is focused on the rear side of the nozzle [figure 4(b)]. This is related to the acceleration mechanism based on density

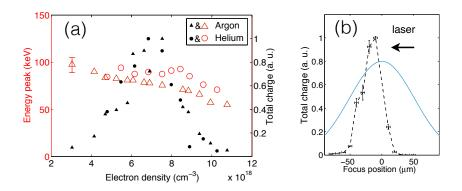


Figure 4. (a) Measured electron beam charge and peak energy over a range of plasma densities. The peak energy is computed from the weighted average energy over a spectral width at 90% of the maximum. (b) Electron charge measured by Lanex signal versus laser focus position relative to the center of the capillary nozzle. Z < 0 means laser is focused on the rear side of the nozzle. The blue line is the shape of a Gaussian density profile with a FWHM of $120 \,\mu$ m.

downramp injection [16], which will be discussed in detail in the next section.

3. Simulation and discussion

To study the acceleration mechanisms, we performed both two- (2D) and threedimensional (3D) particle-in-cell (PIC) simulations using the OSIRIS 2.0 framework [26]. The 2D simulations ran in a stationary window of 713 μ m × 38 μ m, with a grid size of 18000 × 600 cells. A Gaussian profile of neutral helium gas was used with the peak centered at 200 μ m [see the lineout in figure 5(b)]. The peak atomic density was 0.005 n_c , where the plasma critical density n_c is 1.7×10^{21} cm⁻³ for 800 nm light. The peak width (FWHM) was 120 μ m, as determined from the interferometric measurement (figure 1). Electrons were produced using the Ammosov-Delone-Krainov (ADK) ionization model [27], with 4 particles-per-cell in each dimension (i.e. 16 total). The laser parameters were chosen to match our experiment and consisted of a Gaussian spatial profile with a waist of $w_0 = 2 \,\mu$ m, and a 5th order polynomial temporal profile similar to a Gaussian with a pulse duration of $t_p = 32$ fs. The laser pulse leading edge was initialized at 25 μ m and focused at 210 μ m. The simulation ran for 3 ps.

The short laser pulse generates large amplitude plasma waves by its ponderomotive force as it propagates through the center of the gas, but not initially to wave-breaking amplitude. Some time after the laser pulse leaves the plasma, wave-breaking of the plasma waves is observed and electrons are trapped and accelerated. The reason for this trapping is that the plasma waves formed on the downramp of the gaussian profile have a time varying phase velocity v_{ph} . The discussion of plasma oscillations in a nonuniform plasma dates back to the analysis of phase mixing by Dawson in [29]. In a 1D inhomogeneous plasma, the wave number k_p of a plasma wave varies in time according to $\partial k_p/\partial t = -\partial \omega_p/\partial x$ [30]. For an appropriately directed travelling

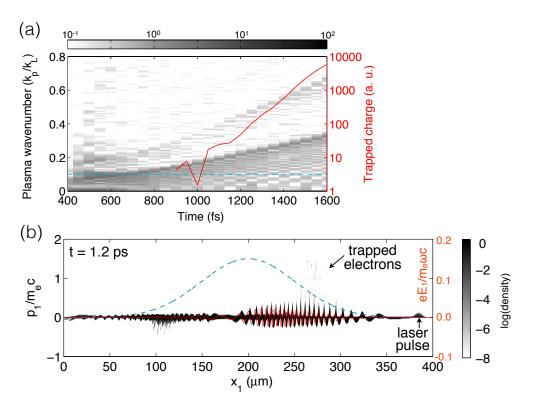


Figure 5. (a) The evolution of plasma wave number spectrum from the 3D PIC simulation. Solid curve (red) is the total charge of the trapped electrons defined as those with $p_e/m_ec > 0.2$ which corresponds to a kinetic energy of about 10 keV. (b) The electron momentum phase-space (x_1, p_1) at t = 1.2 ps. Dashed curve (blue) is a lineout of the Gaussian density profile. Solid curve (red) is the normalized on-axis longitudinal electric field E_1 . The laser travels from left to right.

wave on a decreasing density, k_p increases so that the phase velocity v_{ph} decreases as $v_{ph}/c = [1 + (\zeta/k_p)dk_p/dx]^{-1}$, where $-\zeta = ct - x$ is the distance behind the driver pulse. When the wave phase velocity falls below the maximum electron oscillation velocity in the wake, the charge sheets cross and trapping (wave-breaking) commences [16]. The phase velocity keeps decreasing as the distance behind the pulse becomes larger, so electron trapping in a gradual density inhomogeneity can occur several plasma periods behind the driver laser pulse [31].

The observed trapping mechanism from PIC simulations is illustrated in figure 5. The slowdown of the plasma wave phase velocity can be visualized by plotting the Fourier transform of the electron number density on the central axis as a function of time. Qualitatively identical results are obtained in both 2D and 3D PIC simulations and figure 5(a) is for the 3D simulation result. The peak electron density $n_e = 0.01n_c$ in this simulation translates to a relativistic plasma wave number $k_p = 0.1k_L$ [blue dashed line in figure 5(a)] for a linear plasma oscillation, where $k_L = 2\pi c/\lambda_L$ is the laser wave number in vacuum. In figure 5(b), we plot the electron phase space showing the injected electrons being accelerated from 2D PIC simulations. Note at this time the

Experiment parameter	Low power	High power (Geddes, <i>et al.</i> [17])
Laser pulse energy (mJ)	8	500
Laser pulse FWHM duration (fs)	32	47
Laser peak power (TW)	0.25	10
Laser repetition rate (Hz)	500	10
Focal spot FWHM (μm)	2.5	7.5
Electron kinetic energy (keV)	100	400
Absolute energy spread ΔE (keV)	20	140
Bunch charge	$10 \ fC$	0.3-1 nC
Averaged beam current	5 pA	3-10 nA
RMS shot-to-shot charge stability	< 15%	40%
Plasma peak density (cm^{-3})	$\sim 10^{19}$	$2.2\pm0.3\times10^{19}$
Plasma density FWHM (μm)	100-200	750 ± 100

Table 1. A quantitative comparison between the present and previous work.

leading edge of the laser pulse has travelled to $392 \,\mu m$. Electron trapping occurs about ten plasma waves behind the laser driver around $270 \,\mu m$, where the phase velocity of the plasma waves in the simulation has slowed down to 0.35c. This distinguishes the present work from previous experiments on higher power laser systems, where most electrons are trapped in the few plasma wave buckets just following the driver pulse (e.g. see figure 5A in [17]). A quantitative comparison with the previous experiment using plasma density gradient by Geddes *et al.* [17] is given in table 1 for the other parameters. The time evolution of the wakefield is the crucial reason for the electron trapping at low laser power. Using the cold, non-relativistic upper limit for the wave breaking in the one-dimensional approximation $E_{max} = m_e \omega_p v_{ph}/e$ [29], the calculated value is $eE_{max}/m_e\omega_L c \approx 0.022$, which is slightly larger than the simulated value 0.016 [see figure 5(b)]. The lower trapping threshold observed in our 2D PIC simulations might be due to the fact that the plasma has a finite temperature [32] or could also be due to multi-dimensional effects which can relax the trapping threshold [29]. Equivalent 1D PIC simulations we ran confirm that the 1D trapping condition agrees with the analytical expression very well.

A close-up view of the region where trapping occurs is shown in figure 6 for the 2D PIC simulation. At wave-breaking locations, the plasma wake phase front develops a backward curvature due to the radial dependence of plasma wavelength for the wave evolution (see supplementary movie 1 in [28]). Electrons are trapped along the curved wavefront as shown in figure 6(b)(c). This is different from what is normally observed in laser wakefield acceleration experiments where the electrons are trapped in the few wakes just following the driver laser pulse. In our scenario, the trapped electrons experience a defocusing electric field in the accelerating phase [see figure 6(a)]. These trapped electrons subsequently obtain a sub-relativistic net energy gain in the slow waves. The backward curvature of the plasma waves may explain the "ring" shape of the measured

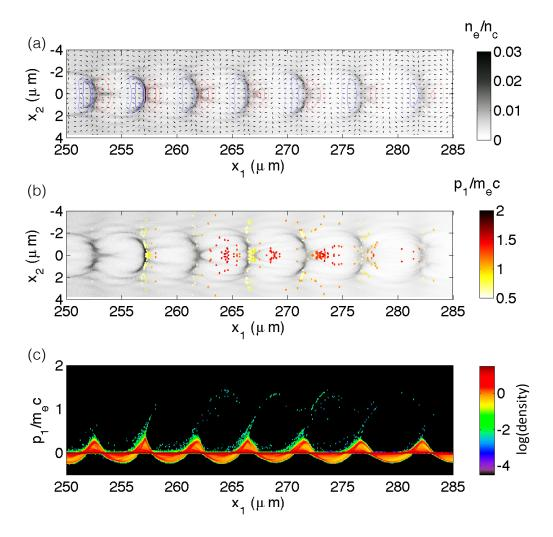


Figure 6. Simulation results from 2D PIC at 1.2 ps in the trapping region (zoomed) of figure 5(b). The laser travels from left to right. (a) Electron density and electric field in space x_1 - x_2 . Black arrows represent the electric field direction. The magnitude of longitudinal electric field E_1 is indicated by the isocontours, where the red (blue) colour corresponds to an accelerating (decelerating) field for electrons. (b) Spatial distribution of the accelerated electrons in x_1 - x_2 . Colour represents the electron longitudinal momentum p_1 . (c) Electron phase space (x_1, p_1) .

electron beam profile. In the experiments, the electron beam profile was found to be sensitive to the configuration of the deformable mirror. A realistic focusing condition with active deformable mirror is likely to break the radial symmetry and seed electron trapping such that the accelerated electrons are preferably distributed in a few stable beamlets [figure 2(b)].

At later times, the longitudinal electric field established by the space charge separation pulls electrons with lower energies back to the plasma, but the portion of the trapped electrons having kinetic energies greater than the electric potential escape as illustrated in figure 7(a) and also in supplementary movie 2 [28]. It should be noted that the electrostatic field in 2D geometry may be overestimated compared to full 3D case

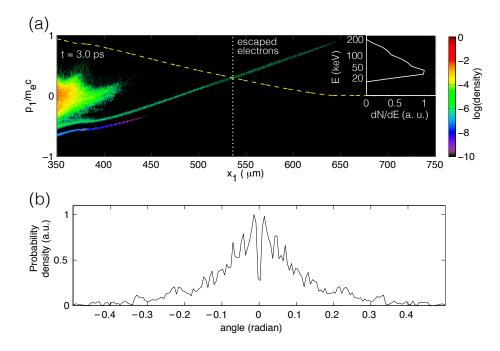


Figure 7. (a) The electron phase space (x_1, p_1) at t = 3.0 ps. Dashed curve (yellow) is the plot of the additive inverse of the longitudinal electric potential expressed in $sgn(\phi)\sqrt{(|\phi|/m_ec^2+1)^2-1}$. The energy distribution of the escaped electrons defined as those with $E + \phi > 0$ is shown in the inset. (b) Angular distribution of the escaped electrons in the simulation.

because it is proportional to inverse distance rather than inverse distance squared. The angular distribution of these electrons shown in figure 7(b) exhibits a bimodal shape with a local minimum on axis, which resembles the observed "ring" structure with a divergence angle of 0.05 radians [see figure 2(a)]. As the accelerated electrons leave the simulation box, they expand longitudinally and its phase space distribution evolves into a linear form [figure 7(a)], indicating a correlation between momentum and position. In principle, one can reverse this chirp to its uncorrelated original duration using techniques such as alpha magnet [33] or radio-frequency cavities [34]. One possible path to further increase the energy energies is to add a second plasma segment of as the accelerator stage, which is not a trivial task, as pointed out by Trines *et al.* [35]. An additional laser pulse may be required to drive a plasma wakefield in the second stage due to the rapid diffraction of the original laser pulse in a tightly focusing scheme. The increased complexity provides more flexibility on the control of the injector phase for optimization of acceleration.

The maximum electron density at the maximum of the Gaussian profile was varied using $n_e/n_c=0.005$, 0.00725, 0.01 and 0.02 in the 2D simulations. The corresponding mean energies of the escaped electrons are 120, 100, 75 and 40 keV, which reproduces the observed experimental trend [figure 4(a)]. By scanning the focus position in the simulations, the maximum number of escaped electrons was generated when focusing between 40 μ m and 60 μ m behind the density peak on the rear side, qualitatively consistent with the experimental results.

4. Conclusion

In conclusion, we have used a high repetition rate 8 mJ short-pulse laser to demonstrate plasma wakefield acceleration of electrons. Highly stable and reproducible electron beams with a quasi-monoenergetic spectrum in excess of 100 keV can be produced. Numerical simulations indicate the electrons are trapped and accelerated to subrelativistic energies in slow plasma waves. With the capability of operation at 500 Hz, "real-time" optimization and control of the electron beam characteristics such as charge and divergence can be realized using adaptive optics. In addition to demonstrating the scalability of wakefield acceleration to lower energies, such a source may be useful for ultrafast electron diffraction applications.

Acknowledgments

This work was supported by the NSF/DOE under grant (PHY-09-03557). The authors acknowledge support from Army Research Office (award W911NF11-1-0-116), DNDO and DARPA. The authors would like to acknowledge the OSIRIS consortium (UCLA/IST Portugal) for the use of the OSIRIS 2.0 framework. Simulations were performed on the Nyx Cluster at the University of Michigan.

Reference

- [1] T. Tajima and J. M. Dawson, Phys. Rev. Lett., 43, 267 (1979).
- [2] S. P. D. Mangles *et al.*, Nature **431**, 535 (2004).
- [3] C. G. R. Geddes *et al.*, Nature **431**, 538 (2004).
- [4] J. Faure *et al.*, Nature **431**, 541 (2004).
- [5] C. Rechatin *et al.*, Phys. Rev. Lett., **102**, 164801 (2009).
- [6] E. Brunetti, et al., Phys. Rev. Lett., 105, 215007 (2010).
- [7] W. P. Leemans, et al., Nat. Phys. 2, 696 (2006).
- [8] S. Kneip et al., Phys. Rev. Lett., 103, 035002 (2009).
- [9] D. H. Froula *et al.*, Phys. Rev. Lett., **103**, 215006 (2009).
- [10] C. Joshi, et al., Phys. Rev. Lett., 47, 1285-1288 (1981).
- [11] N. E. Andreev, et al., Plasma Phys. Reports, 21, 824-834 (1995).
- [12] K. Nakajima, et al., Phys. Rev. Lett., 74, 4428–4431 (1995).
- [13] A. Modena, et al., Nature, **377**, 606-608 (1995).
- [14] A. Ting, et al., Phys. Plasmas, 4, 1889-1899 (1997).
- [15] A. Pukhov and J. Meyer-ter-Vehn, Appl. Phys. B-Lasers Opt., 74, 355, (2002).
- [16] S. Bulanov, et al., Phys. Rev. E 58, R5257 (1998).
- [17] C. G. R. Geddes, et al., Phys. Rev. Lett., 100, 215004 (2008).
- [18] J. Faure, et al., Phys. Plasmas, 17, 083107 (2010).
- [19] K. Schmid, et al., Phys. Rev. ST Accel. Beams 13, 091301 (2010).
- [20] R. Srinivasan, V. A. Lobastov, C. Y. Ruan, and A. H. Zewail, Helv. Chim. Acta 86, 1763 (2003).
- [21] V. A. Lobastov, et al., Proc. Natl. Acad. Sci. U.S.A. 102, 7069 (2005).
- [22] S. Tokita, et al., Appl. Phys. Lett., 95, 111911 (2009).
- [23] A. Mordovanakis, et al., Phys. Rev. Lett., 103, 235001 (2009).

- [24] K. Tanaka, et al., Rev. Sci. Instrum, 76, 013507 (2005).
- [25] Esarey E, et al., IEEE Trans. Plasma Sci. 24 252 (1996).
- [26] R. A. Fonseca, et al, in Computational Science-ICCS 2002, Lecture Notes in Computer Science, Vol. 2331: 342–351 (2002).
- [27] M. V. Ammosov, N. B. Delone, and V. P. Krainov, Sov. Phys. JETP 64, 1191 (1986).
- [28] Supplementary data. See "movie1.mov" and "movie2.mov".
- [29] J. M. Dawson, Phys. Rev. **113**, 383 (1959).
- [30] G. B. Whitham, Linear and Nonlinear Waves (Wiley, New York, 1974).
- [31] A. V. Brantov, et al., Phys. Plasmas, 15, 073111 (2008).
- [32] T. Katsouleas and W. B. Mori, Phys. Rev. Lett., 61 1 (1988); J. B. Rosenzweig, Phys. Rev. A 38, 7 (1988); A. Bergmann and P. Mulser, Phys. Rev. E, 47, 5 (1993).
- [33] P. Kung, et al., Phys. Rev. Lett., 73, 7 (1994).
- [34] S. B. van der Geer, et al., Phys. Rev. ST Accel. Beams 9, 044203 (2006).
- [35] R. M. G. M. Trines, et al., New J. Phys., 12, 045027 (2010).